

An Experimental Study Measuring the Image Field Angle of an Electron Beam Using a Streak Tube

Houzhi Cai ^{1,2}, Xuan Deng ^{1,2}, Lihong Niu ^{1,2}, Qinlao Yang ^{1,2} and Jingjin Zhang ^{1,2,*}

¹ Key Laboratory of Optoelectronic Devices and Systems, Ministry of Education and Guangdong Province, Shenzhen 518060, China

² College of Physics and Optoelectronic Engineering, Shenzhen University, Shenzhen 518060, China

* Correspondence: zhangjingjin@szu.edu.cn

Abstract: The final stage of an inertial confinement fusion (ICF) experiment requires the diagnostic instruments to have the ability to obtain multiple images with high spatiotemporal resolution due to its extremely short duration. However, the influence of field curvature in the streak tube may lead to resolution differences between each image from single line-of-sight (SLOS) technology. In order to achieve high-precision adaptive adjustments, the direction and depth of adjustment should be determined rapidly, which means that the diagnostic instrument must work within the image depth of field of its detector imaging system, requiring it to measure the image field angle of the electron beam. Here, a method based on the streak tube using the combination of planar and spherical fluorescent screens to directly calculate the image field angle of the electron beam from the rear image quality has been proposed for the first time, and its effectiveness has been proved by experiments. It is expected to provide a basis for the diagnostic equipment in ICF experiments to achieve adaptive high-precision adjustment of the focusing voltage to obtain a series of high-resolution images.

Keywords: ICF experiments; streak tube; electron beam; image field angle



Citation: Cai, H.; Deng, X.; Niu, L.; Yang, Q.; Zhang, J. An Experimental Study Measuring the Image Field Angle of an Electron Beam Using a Streak Tube. *Photonics* **2023**, *10*, 267. <https://doi.org/10.3390/photonics10030267>

Received: 19 January 2023

Revised: 28 February 2023

Accepted: 2 March 2023

Published: 3 March 2023



Copyright: © 2023 by the authors. Licensee MDPI, Basel, Switzerland. This article is an open access article distributed under the terms and conditions of the Creative Commons Attribution (CC BY) license (<https://creativecommons.org/licenses/by/4.0/>).

1. Introduction

Inertial confinement fusion (ICF) is a potential method for obtaining energy in the future and is also the principal method for obtaining theoretical and experimental data for thermonuclear weapons [1–3]. The object of ICF research is the high-temperature and high-density plasma produced by the target. The measurement of plasma density, temperature and its change is performed via ultra-fast diagnostic technology [4,5]. Due to the requirement of high spatial and temporal resolution, diagnostic technology is indispensable in obtaining measurements which form the basis for analysing the fusion process. As the experiment progresses, the requirements for ultrafast diagnostic technology also increase [6,7]. The X-ray framing camera is an important ultrafast diagnostic tool, which can be used in ICF, Z-pinch plasma, synchrotron radiation and other experiments [8–10]. In the ICF experiment, the X-ray framing camera is the most effective diagnostic equipment for the symmetrical compression and instability of the target. It can intuitively describe the formation and evolution of the ICF implosion hot spot, providing a basis for judging whether the ICF experiment has reached ignition. It is an indispensable diagnostic tool for studying the motion law of the critical interface, interface instability, and the uniformity of the radiation field [11,12].

Presently, one of the principal methods for observing hot spots is the pinhole array (or Kirkpatrick–Baez mirror microscope) with X-ray traveling wave gated framing imaging technology [13]. The number of frames of such framing cameras is determined by the number of pinholes in the pinhole array at the front end. Because the pinholes in the pinhole array are distributed, each pinhole corresponds to a different azimuth of the measured target. The difference between azimuth angles increases with the increase in the number of

pinholes; thus, single-view frame imaging of the target cannot be achieved. Using this kind of framing camera to diagnose the internal hot spot causes the light emitted from the same point in the target to appear at different positions on different frames, resulting in framing images that cannot accurately judge the evolution process of implosion, which seriously affects the accuracy of the measurements.

In response to this problem, the Livermore Laboratory in the United States has proposed a single line-of-sight (SLOS) framing technology based on the streak tube [14–16], which can achieve strictly SLOS framing. However, limited by the framing principle of mechanical cutting and the size of the electron beam spot, this technology can only achieve four framing images at present. For obtaining more framing images, in addition to upgrading the structure of the image analyser to nine or sixteen squares, it is important to increase the waist size of the electron beam.

SLOS technology uses microchannel plate (MCP) traveling wave gating technology as the back end to achieve framing, so the temporal resolution is related to the exposure time of MCP gating technology. If temporal domain broadening technology is used [17–20], the temporal resolution can reach up to 5 ps; thus, the static spatial resolution of the streak tube should be assigned more importance. The electronic waist and imaging quality in the electronic optical imaging system stand in contradiction: a large waist increases the field curvature, and the final image resolution is different once the focusing voltage is fixed, therefore the higher the number of frames, the greater the difference between images. For the later stage of ICF experiments, implosion time lasts approximately 100 ps; therefore, as many clear images as possible should be collected. Ideally, the focusing voltage should be adjusted during the acquisition of each image to achieve the best resolution. However, this operation requires high-precision and rapid adjustment which cannot be achieved manually, thus requiring adaptive adjustment: feedback from the online quality evaluation of the image is used to control the hardware. This requires ensuring that the adjustment direction is correct and that the final matching position is within the range of high spatial resolution.

It is known that the Petzval image plane of the imaging system is nonlinear due to the existence of the field curve. Therefore, when selecting the final imaging position, it is often necessary to take into account the image definition on the entire imaging plane. In the diagnosis of the ICF experiment, considering the limited transmission speed inside the control element, prompt completion of the adaptive at high precision requires the rapid judgement of the adjustment direction and depth. This requires making the diagnostic instrument work within the depth of field of its detector imaging system at the final adjustment. In fact, the depth of field is the image's square angle corresponding to the electron beam in its electronic optical imaging system. Therefore, to achieve instant adaptive adjustment, the image's square angle of the electron beam must be measured.

Here, a method based on the streak tube has been proposed for the first time, which uses the combination of planar and spherical fluorescent screens to directly calculate the image field angle of the electron beam from the images, providing a basis for the diagnostic equipment to achieve high-precision adaptive adjustment of the focusing voltage to obtain high-resolution series images.

2. Test Principle

Figure 1 shows the testing principle. Although the shape of the image plane shifts and deforms due to the influence of the geomagnetic field [21], which inevitably leads to the unsymmetrical off-axis height corresponding to the intersection point of the image point and fluorescent screen, this does not affect the effectiveness of the method proposed here. This is because the image used in the calculation is the result of a combination of various influencing factors (including the effectiveness of aberrations and geomagnetic field and the coulomb repulsion between charges), which also highlights the robustness of the proposed method. Therefore, any position may be taken for calculation. For comparison, as shown in Figure 1, two points with different off-axis heights have been selected.

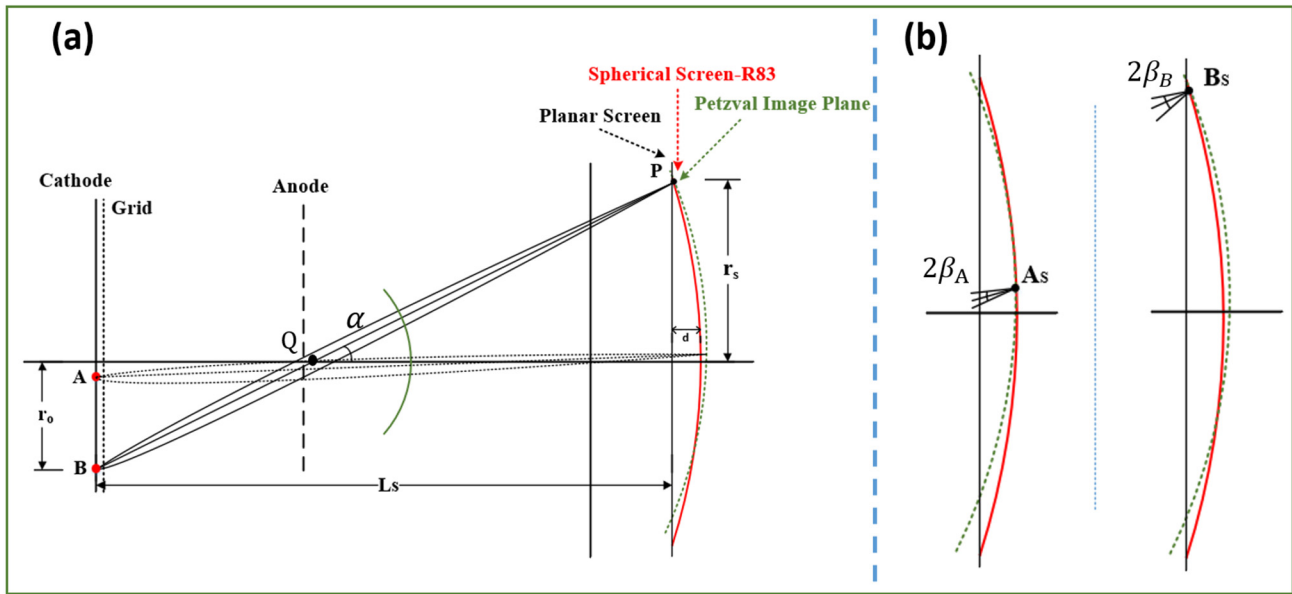


Figure 1. Test schematic diagram: (a) Test example; (b) A/B points focus best.

The following may be obtained from the geometric relationship in Figure 1:

$$R_p = R_s + (4 - d) \times (tg(\alpha + \beta) - tg(\alpha - \beta)), \tag{1}$$

where R_s is the spot diameter on the spherical fluorescent screen, R_p is the spot diameter on the plane fluorescent screen and d is the distance between the spherical screen and the plane screen, as shown in Figure 1a. α is the elevation angle between the intersection point Q of the electron beam and the axis emitted by the image height on the fluorescent screen relative to the corresponding height, β is half of the opening angle of the beam spot to point Q on the fluorescent screen, as shown in Figure 1.

On expanding the trigonometric formula in Equation (1), we obtain,

$$R_p = R_s + 2 \times (4 - d) \times tg\beta \times \frac{(1 + tg^2\alpha)}{(1 - tg^2\alpha * tg^2\beta)}, \tag{2}$$

which implies,

$$\beta = atg\left(\frac{\sqrt{4K_1^2tg^2\alpha + K_2^2} - K_2}{2 \times K_1 \times tg^2\alpha}\right); \tag{3}$$

$$\begin{cases} K_1 = R_p - R_s \\ K_2 = 2 \times (4 - d) \times (1 + tg^2\alpha) \end{cases} \tag{4}$$

From Figure 1:

$$tg\alpha = \frac{(1 + M) \times r_0}{(L_s - d)} \tag{5}$$

And according to the formula [22]

$$d/mm = 83 - \sqrt{83^2 - r_s^2}, \tag{6}$$

where the value of 4 mm is the calculated result of using the formula of the spherical sector with $r_{s_{max}} = 25.5$ mm, which is the radius of the spherical screen with an 83 mm radius of curvature.

3. Experimental Equipment

Here, we have used two kinds of fluorescent screens: a planar fluorescent screen and a spherical fluorescent screen with a radius of curvature of 83 mm. The purpose of using two kinds of fluorescent screens is to use the shape function of the spherical fluorescent screen to determine the parameters to be measured. For example, from the centre of the image point at any position on the spherical screen, the image height and the corresponding transverse magnification can be calculated from the spherical defect formula. Simultaneously, when the A/B image points on the spherical fluorescent screen are adjusted to the corresponding minimum, and the corresponding beam spot size is measured after replacing the plane fluorescent screen under the focusing voltage, then the corresponding beam spot diameter is calculated [23] through the modulation transfer function, and then the corresponding image field angle β is calculated according to Equations (1)–(6).

In Figure 1, the red curve depicts a spherical fluorescent screen with a radius of curvature of 83 mm, an effective diameter of 52 mm, and an eye point height of 4 mm. The structure diagram is shown in Figure 2. The input surface is spherical, and the output surface is made to be planar by processing the optical fibre panel through the outsourcing of Jiangsu Nantong Jingsheng Optical Instrument Co., Ltd. [24]. The S20 phosphor was prepared on the input surface using the centrifugal concentration method.

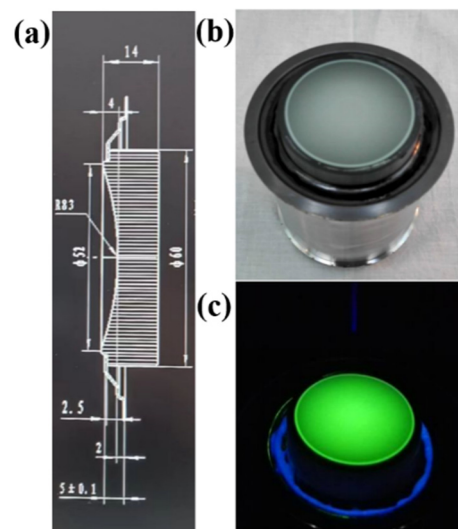


Figure 2. R83 mm spherical fluorescent screen: (a) structure diagram; (b) fluorescent screen assembly drawing; (c) luminous condition of fluorescent screen.

The streak tube used in this test has a six-electrode five-lens structure. The role of each electrode is shown in Figure 3. The whole tube is 430 mm long, the transverse magnification is $M = -1.34$, the total anodic acceleration voltage is 12 kV, and the effective diameter of the photocathode is 30 mm. These structural parameters are shown in Table 1.

Table 1. Parameters of streak tube.

Tube Length (mm)	Diameter (mm)	Magnification	Total Voltage (kV)	Length of Photocathode (mm)	Length of Focus Scope (mm)
430	60	-1.34	12	30	205

The reticle pattern used in the test is shown in Figure 4. Its overall length is 30 mm, and it is divided into four modules. The central part is 15 lp/mm, and the resolution of the left and right sides is 10 lp/mm. The metal chromium reticle was processed and manufactured using an outsourcing method by Shen Zhen Lu Wei Optoelectronics Co.,

Ltd. [25]. The reticle was used to generate the corresponding pattern on an aluminium film substrate through ultraviolet photolithography. Then, styrene was coated on the pattern to form a supporting film. Subsequently, an 80 nm thick Au coating was formed by electron beam evaporation. The developed photocathode is shown in Figure 4. During the experimental test, point A/B in the region was selected to collect data near the best-focused neighborhood on the spherical screen. An image of the cathode can be found in the lower right corner of Figure 4.

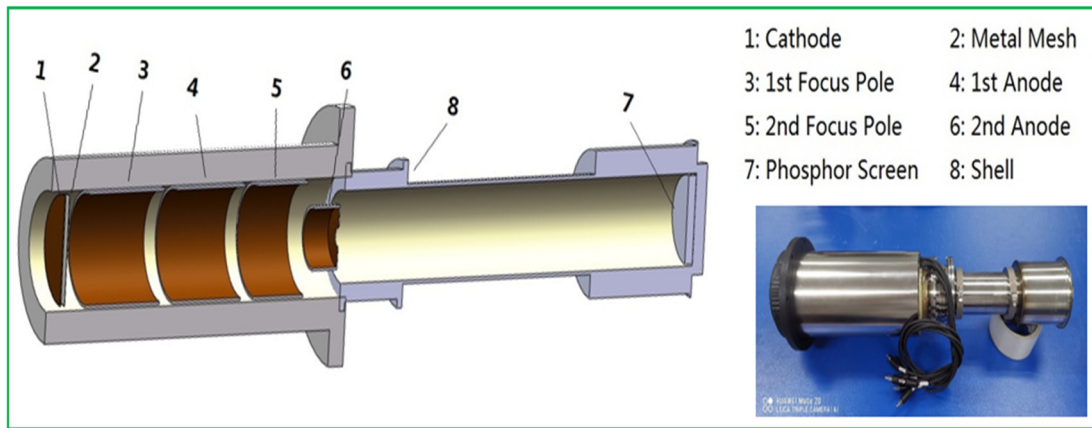


Figure 3. The structure and physical image of the streak tube used in the test: on the left is the internal structure diagram of the streak tube and in the lower right corner is the physical image of the streak tube.

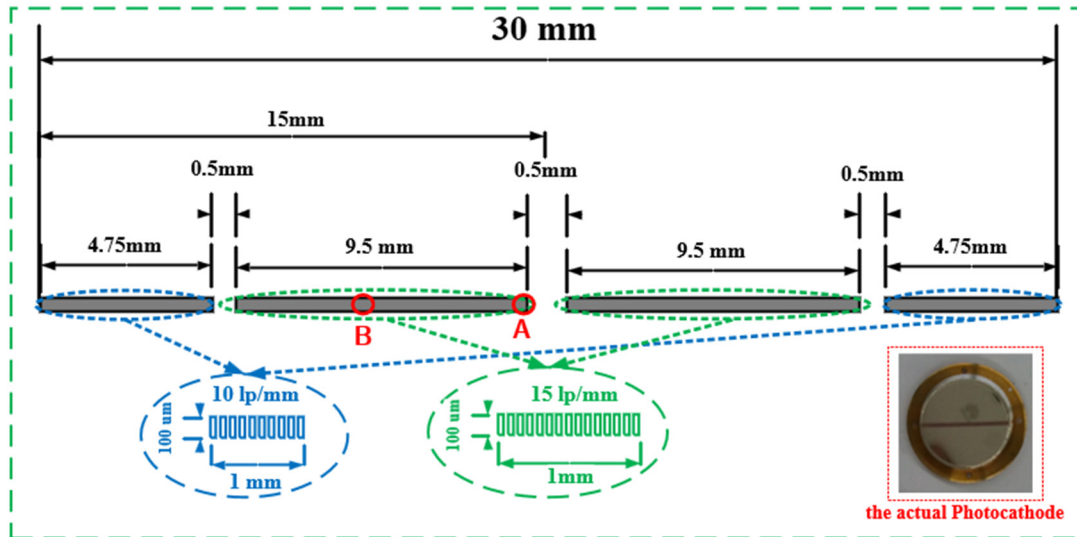


Figure 4. A schematic diagram of the reticle pattern: The spatial resolution of the two parts with the center length of 9.5 mm is 15 lp/mm, as marked by the green text in the figure. The two sides are 10 lp/mm, as shown in the blue text and accompanying schematic diagram in the figure. In the lower right corner is the physical image of the prepared photocathode.

4. Experimental Test and Analysis

Since we have only considered the static working condition of the streak tube, the light source does not need to have information on the time series. Hence the light source used in the verification test experiment is, simply, an ultraviolet lamp. The electrode voltage corresponding to the best resolution of A/B points, when the working condition of the streak tube is adjusted, is shown in Table 2, and the measured fringe pattern is shown in Figure 5.

Table 2. Pole parameters of each scheme.

Scheme	Cathode (kV)	Metal Mesh (kV)	1st Focus Pole (kV)	1st Anode Pole (kV)	2nd Focus Pole (kV)	2nd Anode Pole (kV)	Phosphor Screen (kV)	Shell (kV)
A	−12	−10.5	−6	−1.482	−10.404	−10.382	0	
B					−10.382			

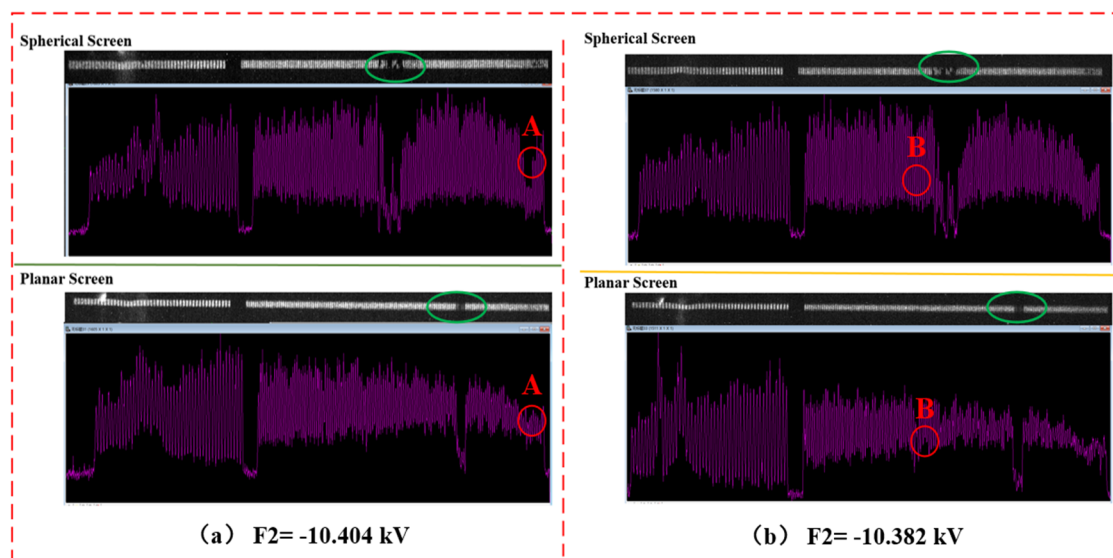


Figure 5. Test result diagram, wherein the upper part is the original fringe image, and the lower part is the corresponding intensity curve: (a) A scheme; (b) B scheme.

It should be noted that the local image marked by the green ellipse in Figure 5 is missing. The main reason is that a mark on the fluorescent screen used was not erased, resulting in the occlusion of the CCD record at this location. Instead, the average value of the valley and peak of the intensity curve was read according to the range marked on the corresponding red circles of A/B points in Figure 5, and then Equations (1)–(6) were used to calculate the results as shown in Table 3.

Table 3. Test results.

Scheme	R_p (μm)	R_s (μm)	Factor K_1	Object Height (mm)	M	D (mm)	Factor K_2 (mm)	β (rad)
A	49.2	28.9	20.3	0.25	1.34	0.00068	8	0.0025
B	48.7	30.1	14.8	5		0.275	7.456	0.00249

In the electronic optical imaging system, the commonly established Lagrangian–Helmholtz relationship is shown in Equation (7).

$$M \times \beta = \frac{\theta \times \sqrt{\epsilon_0 \times \cos^2 \theta}}{\sqrt{\varphi_{total} + \epsilon_0 \times \cos^2 \theta}} \tag{7}$$

where M is the transverse magnification, φ_{total} is the total anode pressure of the striped tube and ϵ_0 is the most probable energy of the photocathode material. For secondary emission electrons, the exit angle of the electron beam at each point on the object surface θ , obeys the Lambert distribution, and for the same photocathode material, its initial energy distribution also follows the Maxwell distribution or Beta distribution. Therefore, the right side of the medium in Equation (7) is constant; in other words, the product of the electron

beam opening angle corresponding to each image point on the Petzval image plane in the entire electronic optical system and the transverse magnification should be equal.

Accordingly, the product of the corresponding electron beam image field angle β in Table 3 and the lateral magnification of the system $M = -1.34$ was found to affirm this, verifying the calculated result.

5. Conclusions

We have proposed a novel method based on the streak tube to directly calculate the image field angle of the electron beam from the phosphor screen image. This method uses the combination of a plane and a spherical fluorescent screen, providing a basis for diagnostic equipment to achieve high-precision adaptive adjustment of the focusing voltage in ICF experiments to obtain a series of high-resolution images.

The final stage of the ICF experiment lasts for an extremely short time; high-precision adaptive adjustment of the diagnostic instrument is required, which should be online, meaning that the hardware cannot be replaced. This also indicates that the shortcomings of this paper are that the proposed method needs to be replaced offline to achieve online measurement, which will be the focus of subsequent research, where an online measurement method will be proposed.

Author Contributions: Conceptualization/Supervision: Q.Y.; Writing—Original Draft Preparation: H.C.; Writing—Review and Editing: L.N.; Software/Formal Analysis: X.D.; Methodology: J.Z.; Funding Acquisition: J.Z. and H.C. All authors have read and agreed to the published version of the manuscript.

Funding: This study was funded by: National Nature Science Foundations of China (NSFC): Nos. 12175153, 12075156; Guangdong Basic and Applied Basic Research Foundation: No. 2021A1515010048; Shenzhen Science and Technology Program: Nos. JCYJ20210324095007020, JCYJ20200109105201936, 20200803105052010.

Institutional Review Board Statement: Not applicable.

Informed Consent Statement: Not applicable.

Data Availability Statement: Data underlying the results presented in this paper are not publicly available at this time but may be obtained from the authors upon reasonable request.

Conflicts of Interest: The authors declare that they have no known competing financial interests or personal relationships that could have appeared to influence the work reported in this paper.

References

1. Betti, R.; Hurricane, O.A. Inertial-confinement fusion with lasers. *Nat. Phys.* **2016**, *12*, 435–449. [[CrossRef](#)]
2. Callahan, D.A.; Hurricane, O.A.; Hinke, D.E.; Ma, T.; Park, H.-S.; Garcia, M.A.B.; Hopkins, L.F.B.; Casey, D.T.; Cerjan, C.J.; Dewald, E.L.; et al. Higher velocity, high-foot implosions on the National Ignition Facility laser. *Phys. Plasmas* **2015**, *22*, 056314. [[CrossRef](#)]
3. Hurricane, O.A.; Callahan, D.A.; Casey, D.T.; Celliers, P.M.; Cerjan, C.; Dewald, E.L.; Dittrich, T.R.; Döppner, T.; Hinkel, D.E.; Hopkins, L.F.B.; et al. Fuel gain exceeding unity in an inertially confined fusion implosion. *Nature* **2014**, *506*, 343–348. [[CrossRef](#)]
4. Danly, C.; Christensen, K.; Fatherley, V.; Fittinghoff, D.N.; Grim, G.P.; Hibbard, R.; Izumi, N.; Jedlovec, D.; Merrill, F.E.; Schmidt, D.W.; et al. Combined neutron and x-ray imaging at the National Ignition Facility (invited). *Rev. Sci. Instrum.* **2016**, *87*, 11D703. [[CrossRef](#)]
5. Bachmann, B.; Hilsabeck, T.; Field, J.; Masters, N.; Reed, C.; Pardini, T.; Rygg, J.R.; Alexander, N.; Benedetti, L.R.; Döppner, T.; et al. Resolving hot spot microstructure using x-ray penumbral imaging (invited). *Rev. Sci. Instrum.* **2016**, *87*, 11E201. [[CrossRef](#)]
6. Pickworth, L.A.; Ayers, J.; Bell, P.; Brejnholm, N.F.; Buscho, J.G.; Bradley, D.; Decker, T.; Hau-Riege, S.; Kilkenny, J.; McCarville, T.; et al. The National Ignition Facility modular Kirkpatrick-Baez microscope. *Rev. Sci. Instrum.* **2016**, *87*, 11E316. [[CrossRef](#)]
7. Hu, S.X.; Michel, D.T.; Davis, A.K.; Betti, R.; Radha, P.B.; Campbell, E.M.; Froula, D.H.; Stoeckl, C. Understanding the effects of laser imprint on plastic-target implosions on OMEGA. *Phys. Plasmas* **2016**, *23*, 102701.
8. Igumenshchev, I.V.; Goncharov, V.N.; Marshall, F.J.; Knauer, J.P.; Campbell, E.M.; Forrest, C.J.; Froula, D.H.; Glebov, V.Y.; McCrory, R.L.; Regan, S.P.; et al. Three-dimensional modeling of direct-drive cryogenic implosions on OMEGA. *Phys. Plasmas* **2016**, *23*, 052702. [[CrossRef](#)]
9. Spears, B.K.; Munro, D.H.; Sepke, S.; Caggiano, J.; Clark, D.; Hatarik, R.; Kritcher, A.; Sayre, D.; Yeamans, C.; Knauer, J.; et al. Three-dimensional simulations of National Ignition Facility implosions: Insight into experimental observables. *Phys. Plasmas* **2015**, *22*, 056317. [[CrossRef](#)]

10. Rosch, R.; Trosseille, C.; Caillaud, T.; Allouche, V.; Bourgade, J.L.; Briat, M.; Brunel, P.; Burillo, M.; Casner, A.; Depierreux, S.; et al. First set of gated X-ray imaging diagnostics for the Laser Megajoule facility. *Rev. Sci. Instrum.* **2016**, *87*, 33706. [[CrossRef](#)]
11. Bose, A.; Woo, K.M.; Betti, R.; Campbell, E.M.; Mangino, D.; Christopherson, A.R.; McCrory, R.L.; Nora, R.; Regan, S.P.; Goncharov, V.N.; et al. Core conditions for alpha heating attained in direct-drive inertial confinement fusion. *Phys. Rev. E* **2016**, *94*, 011201. [[CrossRef](#)]
12. Hilsabeck, T.J.; Frenje, J.A.; Hares, J.D.; Wink, C.W. A stretch/compress scheme for a high temporal resolution detector for the magnetic recoil spectrometer time (MRSt). *Rev. Sci. Instrum.* **2016**, *87*, 11D807. [[CrossRef](#)]
13. Yi, S.-Z.; Si, H.-X.; Huang, Q.-S.; Zhang, Z.; Jiang, L.; Qi, R.-Z.; Zhang, Z.; Wang, Z.-S. Research progress of multi-channel Kirkpatrick–Baez microscope for X-ray diagnostics in laser inertial confinement fusion. *Acta Opt. Sin.* **2022**, *42*, 1134007.
14. Bradley, D.K.; Bell, P.M.; Dymoke-Bradshaw, A.K.L.; Hares, J.D.; Bahr, R.E.; Smalyuk, V.A.; Hargrove, D.R.; Piston, K. Development and characterization of a single-line-of-sight framing camera. *Rev. Sci. Instrum.* **2001**, *72*, 694–697. [[CrossRef](#)]
15. Holder, J.P.; Piston, K.W.; Bradley, D.K.; Bell, P.M.; Dymoke-Bradshaw, A.K.L.; Hares, J.D. Further development of a single line of sight x-ray framing camera. *Rev. Sci. Instrum.* **2003**, *74*, 2191–2193. [[CrossRef](#)]
16. Bradley, D.K.; Holder, J.P.; Damian, C.M.; Piston, K.W.; Bell, P.M.; Dymoke-Bradshaw, A.K.L.; Hares, J.D. Progress on the development of a single line of sight X-ray framing camera. *Rev. Sci. Instrum.* **2004**, *75*, 4054–4056. [[CrossRef](#)]
17. Fu, W.; Cai, H.; Wang, D.; Lei, Y.; Liu, J. Time resolved x-ray image of laser plasma interactions using a dilation framing camera. *Optik* **2019**, *186*, 374–378. [[CrossRef](#)]
18. Cai, H.-Z.; Fu, W.-Y.; Wang, D.; Lei, Y.-F.; Gu, L.; Liu, J.-Y. Large-format pulse-dilation framing tube with 5 lp/mm spatial resolution. *Optik* **2019**, *185*, 441–446. [[CrossRef](#)]
19. Liu, J.; Fu, W.; Deng, P.; Wang, D.; Lei, Y.; Huang, J.; Wang, Y.; Cai, H. Simulation of a pulse-dilation framing tube with sensitive diameter of 60 mm using large aperture short magnetic lens. *Optik* **2019**, *203*, 163974. [[CrossRef](#)]
20. Cai, H.; Fu, W.; Wang, D.; Lei, Y.; Liu, J. Three-strip microchannel plate gated x-ray framing camera. *Sens. Actuators A Phys.* **2018**, *285*, 355–361. [[CrossRef](#)]
21. Zhang, J.-J.; Lei, B.-G.; Yang, Q.-L. Improvement of imaging performance for X-ray streak tube. *J. Shenzhen Univ. Sci. Eng.* **2017**, *34*, 14–19. [[CrossRef](#)]
22. Zhang, J.-J.; Liu, A.-L.; Guo, B.-P.; Yang, Q.-L.; Zong, F.-K. Influence of geomagnetic field on the imaging performance of a streak tube. *Nucl. Inst. Methods Phys. Res. A* **2020**, *950*, 162808.
23. Csorba, I.P. Modulation transfer function of image tube lenses. *Appl. Opt.* **1977**, *16*, 2647–2650. [[CrossRef](#)]
24. Available online: <http://www.optics.cn/> (accessed on 1 March 2023).
25. Available online: <http://www.newwaymask.com/> (accessed on 1 March 2023).

Disclaimer/Publisher’s Note: The statements, opinions and data contained in all publications are solely those of the individual author(s) and contributor(s) and not of MDPI and/or the editor(s). MDPI and/or the editor(s) disclaim responsibility for any injury to people or property resulting from any ideas, methods, instructions or products referred to in the content.